nature communications

Article

https://doi.org/10.1038/s41467-025-58416-y

Mechanically deformable organic ferroelectric crystal with plasticity optimized by fluorination

Received: 28 June 2024

Accepted: 20 March 2025

Published online: 29 March 2025

Check for updates

Pei-Zhi Huang[1,4], Zunqi Liu[2,4], Lou-Kai Ye[1,4], Hao-Fei Ni[1], Jia-Qi Luo[1], Gele Teri[1], Qiang-Qiang Jia[1], Bo Zhuang[3], Chang-Feng Wang[1], Zhi-Xu Zhang[1] ✉, Yi Zhang[1] ✉ & Da-Wei Fu[1,2] ✉

The ability of plastic deformation exerts in bulk crystals would offer great promise for ferroelectrics to achieve emerging and exciting applications. However, conventional ferroelectric crystals generally suffer from inherent brittleness and are easy to fracture. Here, by implementing fluorination on anion, we successfully design a flexible organic ferroelectric phenylethylammonium trifluoromethanesulfonate (PEA-TFMS) with interesting plasticity in its bulk crystals. To our knowledge, it is the first observation since the discovery of organic ferroelectric crystal triglycine sulfate in 1956. Compared to parent PEA-MS (phenylethylammonium mesylate), fluorination subtly alters ionic orientation and interactions to reorganize dipole arrangement, which not only brings switchable spontaneous polarization but also endows PEA-TFMS crystal with macroscopical bending and spiral deformability, making it a competitive candidate for flexible and wearable devices. Our work will bring inspiration for obtaining mechanically deformable organic ferroelectric crystals toward flexible electronics.

Ferroelectrics that characterized by switchable spontaneous polarization enable wide functional applications from information processing, energy conversion to medical detection[1–6]. Since the first discovery of ferroelectricity[7], the past century has witnessed continuous developments in ferroelectrics that have mainly concentrated on the inorganic ones represented by $BaTiO_3$ and $Pb(Zr_{1-x}Ti_x)O_3$ with heavy metals and high hardness[8,9]. Whereas, the new pursuits for more energy-saving, biocompatible, flexible and wearable devices have driven great interest in molecular ferroelectrics over recent years, especially pure organic ones[10,11]. By taking the attributes of facile solution processing, lightweight, structural diversity and tunability, organic ferroelectric crystals also possess unrivalled advantages in material preparation and functional design[12–15]. Due to tight molecular packing or coordinated network, however, most organic ferroelectrics usually exhibit inherent brittleness[16], which restricts crystal deformation and is detrimental to their potential applications in flexible electronics. Mechanically flexible devices rely on the mechanical properties of materials, which should meet the necessary requirements for adaptive deformation in different working environments[17–19]. Notably, a series of excellent plastic molecular ferroelectrics have been reported previously, but their mechanical bending characteristics require implementation in high-temperature paraelectric phases[20–22]. Depositing epitaxial thin films of ferroelectric crystals on polymer substrates has been studied for developing flexible devices, nevertheless, such way suffers from complex preparation processes and possible ferroelectric performance losses[23–25]. To this stage, whether free-standing bulk

[1]Institute for Science and Applications of Molecular Ferroelectrics, Key Laboratory of the Ministry of Education for Advanced Catalysis Materials, Zhejiang Normal University, Jinhua, People's Republic of China. [2]Chemistry and Chemical Engineering College, Xinjiang Agricultural University, Urumqi, People's Republic of China. [3]Ordered Matter Science Research Center, Jiangsu Key Laboratory for Science and applications of Molecular Ferroelectrics, Southeast University, Nanjing, People's Republic of China. [4]These authors contributed equally: Pei-Zhi Huang, Zunqi Liu, Lou-Kai Ye. ✉e-mail: zhangzhixu@zjnu.edu.cn; yizhang1980@seu.edu.cn; dawei@zjnu.edu.cn

ferroelectric crystals can directly achieve plastic deformation without other auxiliary limitations, and thereby purposefully achieving adaptable mechanical shaping for application conditions, remains a long-term pursuit and expectation in ferroelectric field. Admittedly, the plastic deformation of bulk crystals have been extensively studied in various fields[18,26–31]. However, since the first discovery of organic ferroelectric crystal triglycine sulfate in 1956[32], organic one equipped with such abilities remains just an academic interest.

Natural modifiability and diversity of organic molecules have become fertile ground for designing ferroelectrics. Fluorination has emerged as a promising strategy for eliciting or intensifying desirable properties across multiple fields involving energy, catalysis, medicine, etc.[33–36]. In crystal engineering, introducing fluorine atoms can to some extent alter the molecular dipole moment and orientation as well as molecular interactions, thereby affecting crystal symmetry and physical properties[37,38]. For ferroelectricity, its required crystal polarity is closely associated with the internal permanent dipoles and their arrangement in lattice[39–41]. For instance, Zhang et al recently reported a fluorinated organic ferroelectric crystal $HOCH_2(CF_2)_3CH_2OH$, showing high piezoelectric response and good biodegradability that are attractive for biomedical electronics[6]. The H/F substitution strategy has been successfully implemented in ferroelectric design and performance optimization as exemplified by [4-fluoro-quinuclidinium]ReO_4[42], (m-fluoroanilinium)(dibenzo[18]crown-6)[Ni(2-thioxo-1,3-dithiole-4,5-dithiolate)$_2$][43], and $[(CH_3)_3NCH_2F]ZnCl_3$[44]. Emphatically, the introduction of fluorines would have a significant impact on the mechanical properties of crystals. Hayashi et al. implemented fluorination to introduce S-F interactions to extend π-conjugated system, and thereby successfully creating flexibly elastic organic single crystals, whose elastic mechanism is analogous to that of the first elastic crystal[45,46]. But meanwhile, complex molecular interactions and subtle molecular structural distortions also bring great uncertainty and contingency to ferroelectric design and performance regulation. Unravelling intrinsic mechanism and feasible ways to achieve organic ferroelectrics with fascinating plasticity has always been the academic interests.

In this work, we carry out the conventional fluorination strategy on PEA cations of parent PEA-MS, which crystallize in centrosymmetric *I*2/*a* space group, but unfortunately the results are unsatisfactory for all the fluorinated productions with different H/F substitution sites (Fig. 1). It must be pointed out that, towards ferroelectrics, the fluorination strategy is almost always applied to cationic parts in molecular crystals, while its pivotal role in anionic parts has been historically overlooked. In view of this, we pioneer to implement the H/F substitution on anionic parts of ionic molecular crystals, aiming to explore their effects in ferroelectric design (Fig. 1). Compared to parent PEA-MS, excitingly, the fluorinated PEA-TFMS shows crystal polarity with $Pna2_1$ space group, which features two-dimensional hydrogen bonding network in a wave-like pattern. Fluorination cleverly changes ionic orientations and interactions, reorganizing dipole arrangement to create opportunities for switchable spontaneous polarization. More interestingly, fluorination endows PEA-TFMS with remarkable plasticity, that is, its ferroelectric phase exhibits macroscopic bending and spiral deformation under external forces, without recovering upon their removal. This phenomenon represents an unprecedented occurrence among the reported organic ferroelectric crystals to date. Combined with aqueous solution preparation, these attributes make PEA-TFMS an desirable candidate for mechanically flexible and human-wearable devices.

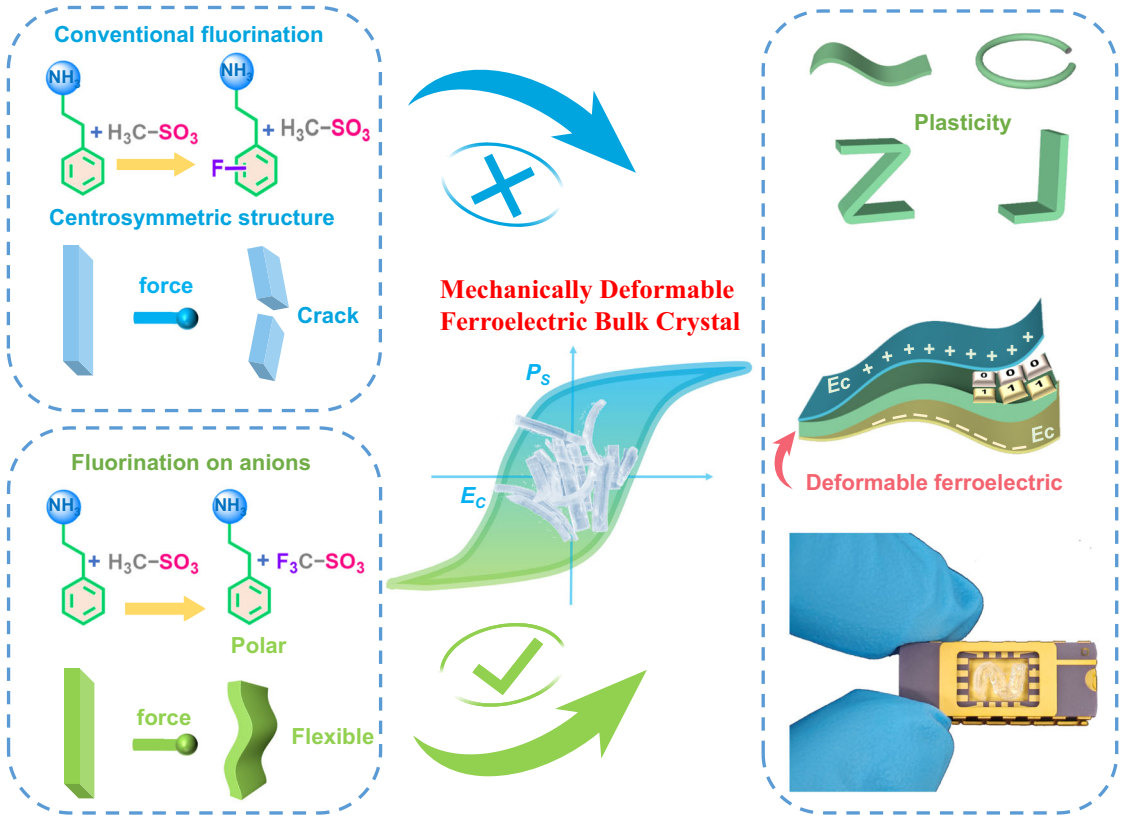

Fig. 1 | Designing strategy. Designing strategy of an organic ferroelectric with mechanical flexibility by implementing fluorination on anionic parts. The blue cartoons at the top left represent cationic fluorinated crystals. The green cartoons at the bottom left and top right represent anionic fluorinated crystals. E_c: Coercive field of spontaneous polarization of ferroelectrics. P_S: Saturation polarization of spontaneous polarization of ferroelectrics. The dimension of the object in the bottom right photo is 20 mm × 7 mm × 2 mm.

https://doi.org/10.1038/s41467-025-58416-y

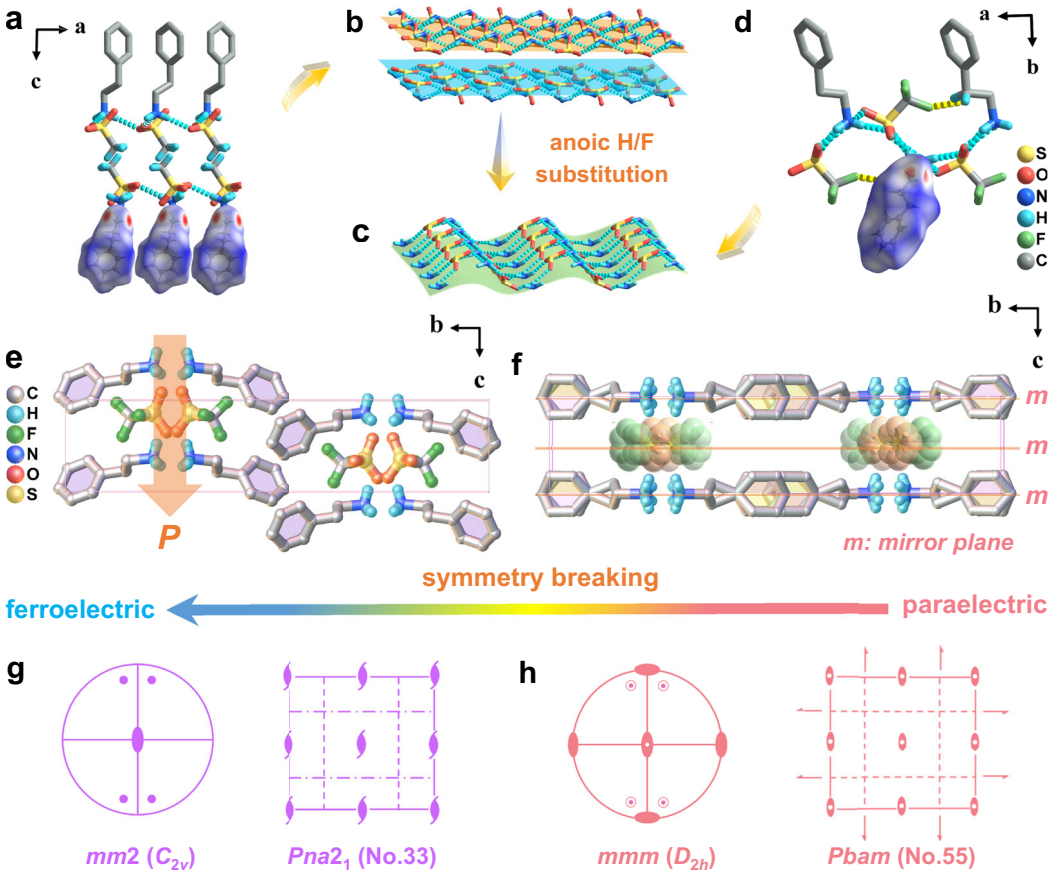

Fig. 2 | Structural information. a Packing structure of PEA-MS viewed along *b*-axis with N – H···O hydrogen bonds (bule bonds). **b-c** Quasi 2D network layers of hydrogen bonds in the structure of PEA-MS (**b**) and PEA-TFMS (**c**). **d** Packing structure of PEA-TFMS viewed along *c*-axis with N – H···O hydrogen bonds (bule bonds) and C – H···F interactions (yellow bonds). **e**, **f** Packing structure of PEA-TFMS viewed along *a*-axis in ferroelectric phase (**e**) and paraelectric phase (**f**). The arrow in (**e**) represent the spontaneous polarization direction. The orange and green spheres in (**f**) represent highly disordered oxygen and fluorine atoms. **g**, **h** Equatorial plane projection of point group and spatial symmetry operations of space groups of ferroelectric phase (**g**) and paraelectric phase (**h**) for PEA-TFMS. Some hydrogen atoms were omitted for clarity. The red-blue-white surfaces in (**a**, **d**) represent the Hirshfeld surfaces of the PEA^+ cations in the crystal structure, with the red points meaning hydrogen bonding interactions.

Results

Structural analysis of crystals

All the crystals are easily prepared by slow evaporation of their respective methanol solutions (Supplementary Note 1). For crystal structure of PEA-MS, interestingly, PEA cations and MS anions are stacked in a layered-like manner along the [001] direction, where two MS layers alternately separate the PEA layers (Fig. 2a). Such arrangement is stabilized by N – H···O hydrogen bonding between N atoms of PEA and O atoms of MS, which form a quasi two-dimensional (2D) hydrogen bonding network (Fig. 2b). The orientation of adjacent PEA layers is opposite to each other, and the same applies to the neighboring MS layers. These structural characteristics of PEA and MS arrays leads to the cancellation of dipole moments, making PEA-MS crystallizes in a centrosymmetric *I2/a* space group (Supplementary Table 1). Given the previous success of the H/F substitution strategy, we implemented this strategy on the PEA cations of the parent PEA-MS, aiming to induce crystal polarity. However, the resulting *o*-FPEA-MS (*o*-fluorophenethylammonium mesylate), *m*-FPEA-MS (*m*-fluorophenethylammonium mesylate) and *p*-FPEA-MS (*p*-fluorophenethylammonium mesylate) maintain the crystal symmetry of the centrosymmetric space group, belong to *Pbca*, $P2_1/n$ and *C2/c* space group respectively (Supplementary Table 2). Moreover, their ionic arrangements are also similar to those of the parent PEA-MS, featuring 2D network with repeating double hydrogen bonding layers (Supplementary Fig. 1).

For ionic molecular crystals, anionic parts are also an indispensable component for determining chemical and physical properties, but they have long been overlooked in terms of designing ferroelectricity. We thus carried out H/F substitution on MS anions of parent PEA-MS, and exhilaratingly, the crystal symmetry of resulting PEA-TFMS transformed into polar $Pna2_1$ space group (Supplementary Table 1). Structurally, PEA-TFMS also adopts a quasi 2D hydrogen bonding network with an alternating stacking arrangement of PEA and TFMS layers (Fig. 2d). But differently, compared to PEA-MS, the repetitive unit of such 2D network of PEA-TFMS changes into a single hydrogen bonding layer, displaying in a wave-like pattern (Fig. 2c). Notably, besides N – H···O hydrogen bonding, anionic fluorination introduces new C – H···F weak interactions, which act like ropes pulling on PEA and TFMS ions to subtly alter the stacking arrangement and orientation of ions (Fig. 2d). From packing view, a striking feature of structure is that both PEA and TFMS are aligned toward the crystallographic *c*-axis direction, which will accumulate dipole moments to generate a macroscopic spontaneous polarization along [001] direction (Fig. 2e).

Thermal analysis revealed that PEA-TFMS experiences a reversible phase transition by observing a pair of endothermic/exothermic peaks at 346/334 K (Fig. 3a & Supplementary Fig. 2a). Five cycles of differential scanning calorimetry (DSC) measurements (Supplementary Fig. 2b) further confirm the good reversibility and cycling stability of PEA-TFMS's phase transition. For clarity, we label the phases below and above the

https://doi.org/10.1038/s41467-025-58416-y

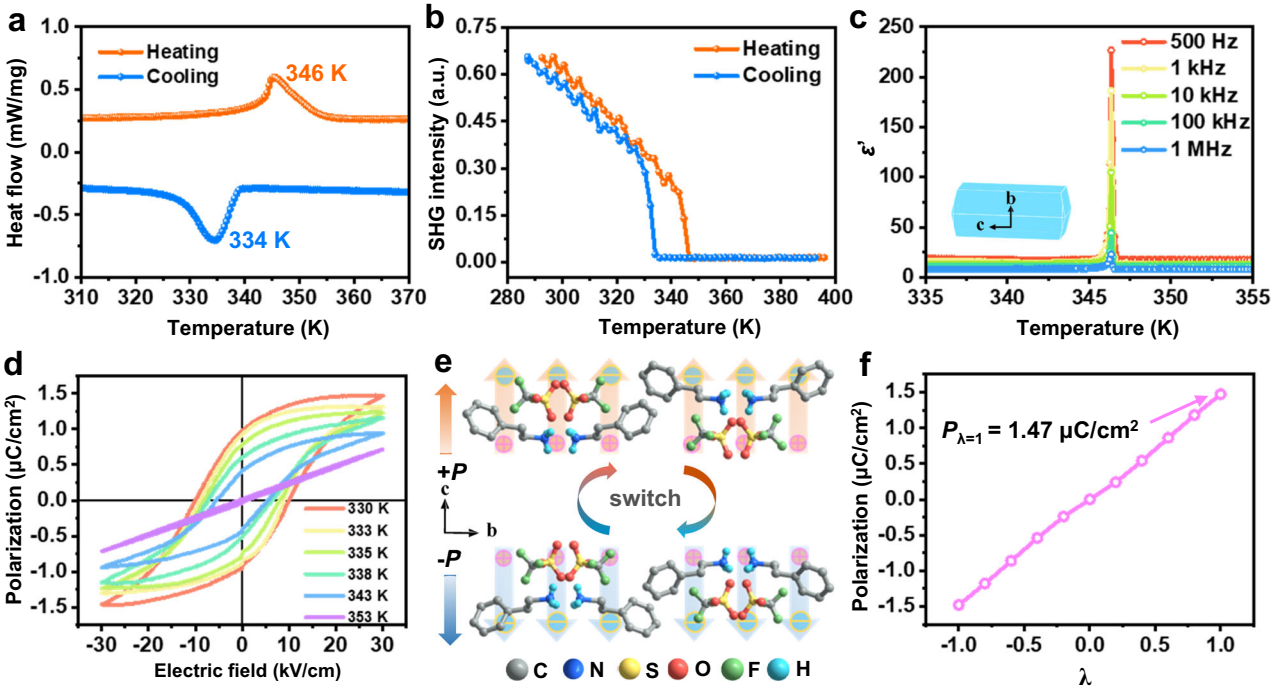

Fig. 3 | DSC, SHG, dielectric properties and ferroelectricity of PEA-TFMS. a DSC curves of PEA-TFMS. DSC: Differential scanning calorimetry. **b** The SHG intensity of PEA-TFMS as a function of temperature. SHG: second harmonic generation. **c** Real part of dielectric constant during the heating process. The blue image is the topography of PEA-TFMS modeled by the crystal structure. **d** *P-E* hysteresis loops measured on the PEA-TFMS crystal. **e** Two ferroelectric states with opposite orientation of polarization. Some hydrogen atoms were omitted for clarity. The arrows represent spontaneous polarization direction. The "+" and "-" signs represent positive and negative charges. **f** Ferroelectric polarization evolution of PEA-TFMS as a function of structure parameter λ.

transition temperature as low-temperature phase (LTP) and high-temperature phase (HTP) respectively. At 353 K in HTP, the structure of PEA-TFMS was determined in the centrosymmetric *Pbam* space group of *mmm* point group (Supplementary Table 1), where some atoms were split to satisfy a good refinement due to the intensified atomic thermal vibration. In lattice, PEA and TFMS ions are situated in a symmetric position of mirror plane that perpendicular to the *c*-axis, making its orientation disordered to offset dipole moment (Fig. 2f). Accordingly, the phase transition mechanism can be ascribed to the joint order-disorder transition of both PEA cations and TFMS anions. As shown in Fig. 2g, h, the Aizu notation for the symmetry breaking is *mmm*F*mm*2.

Characterization of ferroelectricity

We further determined the crystal symmetry of these materials using the second harmonic generation (SHG) technique, which exhibits high sensitivity to the absence of inversion centers, except for 432, 622, and 422 point groups. As shown in Supplementary Fig. 3, the PEA-MS and its cationic modified derivatives with centrosymmetric crystal structures show inactive SHG signal, while non-zero SHG intensity of its anionic fluorination products PEA-TFMS indicate the crystal polarity. The variation trend of SHG response with temperature confirms that the reversible symmetry change from polar $Pna2_1$ to centrosymmetric *Pbam* space group of PEA-TFMS (Fig. 3b). Typical paraelectric-ferroelectric phase transitions are generally accompanied by significant anomalies of dielectric constant. The temperature-dependent dielectric constant of PEA-TFMS exhibits a λ-type mutation peaked at about 346 K (Fig. 3c), as well as the dielectric loss (Supplementary Fig. 4a). Moreover, the dielectric response is consistent with Curie −Weiss law, $1/\varepsilon' \approx (T - T_O)/C$. By fitting this law, the curve shows an obvious jump in the vicinity of T*c* (Supplementary Fig. 4b).

The nonlinear hysteresis relationship between polarization (*P*) and applied electric field (*E*) is one of the most essential characteristics of ferroelectricity. By using Sawyer-Tower method, at 353 K, the measured *P* exhibits a linear relationship with the variation of *E*, conforming to the nature of ordinary dielectrics in paraelectric phase. Below Curie temperature (T_C), the well-defined *P-E* hysteresis loops emerged in the range of 343–330 K, directly demonstrating ferroelectricity of PEA-TFMS (Fig. 3d). As the temperature decreases, the saturation polarization (P_S) value gradually increases to reach about 1.46 μC/cm² at 330 K. Furthermore, density functional theory (DFT) is employed to evaluate the polarization dynamics of PEA-TFMS (Fig. 3e, f), yielding a calculated polarization value of 1.47 μC/cm², which is consistent with the experimental value. Additionally, PEA-TFMS does not show a substantial fatigue effect after 10^7 switching cycles (Supplementary Fig. 5).

Ferroelectric domain dynamics at micro-scale were studied by piezoresponse force microscopy (PFM) technique. The PFM amplitude and phase images of PEA-TFMS thin film show domain structures where different polarization states are separated by clear domain walls, which are independent from topography of the film surface (Supplementary Fig. 6). Selecting a specific region with an initial almost single-domain state (Fig. 4a–c), we successively applying a tip voltage of +120 V and −120 V to examine local polarization switching process. As shown in Fig. 4e, f, h, i, the evolution of color contrast observed in phase image as well as the evident domain wall movement in amplitude image intuitively indicate ferroelectricity of PEA-TFMS. Additionally, the butterfly amplitude loops and 180° phase shifts further demonstrate robust ferroelectric switching (Fig. 4d, g).

Mechanical properties of crystals

The fluorination on anionic parts not only successfully induces ferroelectricity, but also greatly improves mechanical flexibility. Parent PEA-MS exhibits brittleness (Supplementary Fig. 7a), while the fluorinated PEA-TFMS shows remarkable mechanical adaptability and plasticity, allowing for macroscopic bending and even helical deformation without losing its integrity under external stress (Fig. 5a &

https://doi.org/10.1038/s41467-025-58416-y

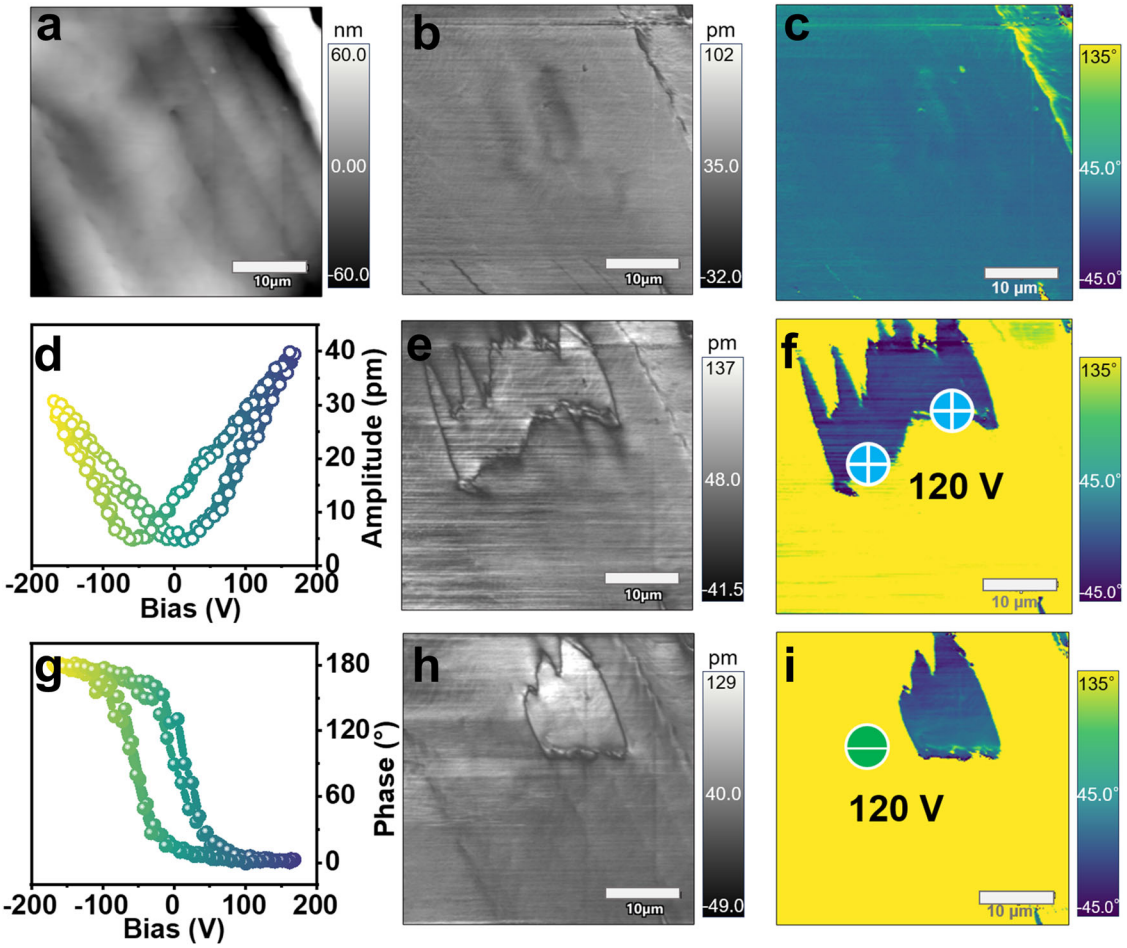

Fig. 4 | Ferroelectric domain structures and polarization switching of PEA-TFMS. a–c PFM images of topography (**a**), amplitude (**b**), and phase (**c**) in the initial state. PFM: Piezoresponse force microscope. **d**, **g** PFM amplitude (**d**) and phase (**g**) signals as functions of the tip voltage. The yellow and dark blue curves represent the spontaneous polarization of the crystal in two opposite directions. **e**, **f**, **h**, **i** Amplitude and phase images after applying tip voltages of +120 V (**e**, **f**) and −120 V (**h**, **i**).

Supplementary Fig. 7b). Single-crystal X-ray diffraction determination was conducted to obtain the crystal structure of bent PEA-TFMS crystal. Compared with original structure, the space group and cell parameters of bent crystal remain unchanged (Supplementary Table 1). The morphology of the crystal's side surface (100), as characterized by scanning electron microscope (SEM) and atomic force microscope (AFM), reveals that both the straight and bent sections exhibit no significant textures on the surface, indicating the integrity of the crystal during the bending process (Fig. 5b–j). Among which, the striped patterns observed in the AFM images of the straight section result from the crystal growth process. Additionally, Raman spectroscopy was also employed to investigate the crystal structure change of bent and unbent PEA-TFMS at a molecular level. As shown in Supplementary Fig. 8, compared with the Raman spectrum of the unbent region, no additional peaks are observed in the bent region, suggesting that the crystal does not become amorphous after bending, which means the molecular arrangement in the crystal structure maintains orientational order and retains the polar alignment. Then, nanoindentation technique was employed to assess the mechanical properties of both PEA-TFMS and PEA-MS crystals, and the load-displacement curves were fitted based on the Oliver-Pharr model to obtain the Young's modulus (E) and hardness (H)[47], as shown in Fig. 5k and Supplementary Fig. 9a–d. The PEA-TFMS crystals present an average Young's modulus (E) of 4.31, 2.18, and 2.07 GPa and hardness (H) of 204.1, 42.1, and 71.4 MPa for (010), (100), and (001) planes, respectively, obviously smaller than those of the parent PEA-MS (10.21 GPa, 482.4 MPa), and presenting favorable competitiveness among organic crystals with an average E and H of 12.05 GPa and 500.0 MPa[48]. Moreover, the value of Young's modulus and hardness of PEA-TFMS are several orders of magnitude lower than those of inorganic ferroelectrics such as $BaTiO_3$ (167.9 GPa, 13.6 GPa)[49], and are close to the organic polymer PVDF (3.28 GPa, 240.3 MPa)[50] (Fig. 5l).

The PEA-TFMS bulk crystal exhibits the rare combination of plasticity and ferroelectricitity (Supplementary Table 3), which has inspired us to further explore its dielectric and ferroelectric properties under bending conditions. As shown in Supplementary Fig. 10, the dielectric constant remains essentially unchanged with the bending of the crystal. Furthermore, the ferroelectric characteristics are still present in the bent crystal, as demonstrated by the obvious P-E hysteresis loops with the value of Ps being 1.31 μC/cm^2, consistent with that of the unbent crystal (Fig. 5m). The bent crystal can be conceptualized as consisting of an infinite number of straight crystals, each with its polar axis rotated at specific angles. The polarization direction of the bent crystal exhibits a component along the "original c-axis", thus allowing spontaneous polarization remains in the bent crystal (Supplementary Fig. 11). Additionally, the PFM measurements were performed on the same position of the PEA-TFMS crystal both before and after bending, as indicated by the circled area in Fig. 6a, e. As shown in Fig. 6b–d, f–h, after bending, clear domain structures remain observable, with a slight shift of domain walls within the bent region. This observation demonstrates that ferroelectricity does not disappear even when the crystal is bent. Based on the plasticity of the ferroelectric crystal PEA-

https://doi.org/10.1038/s41467-025-58416-y

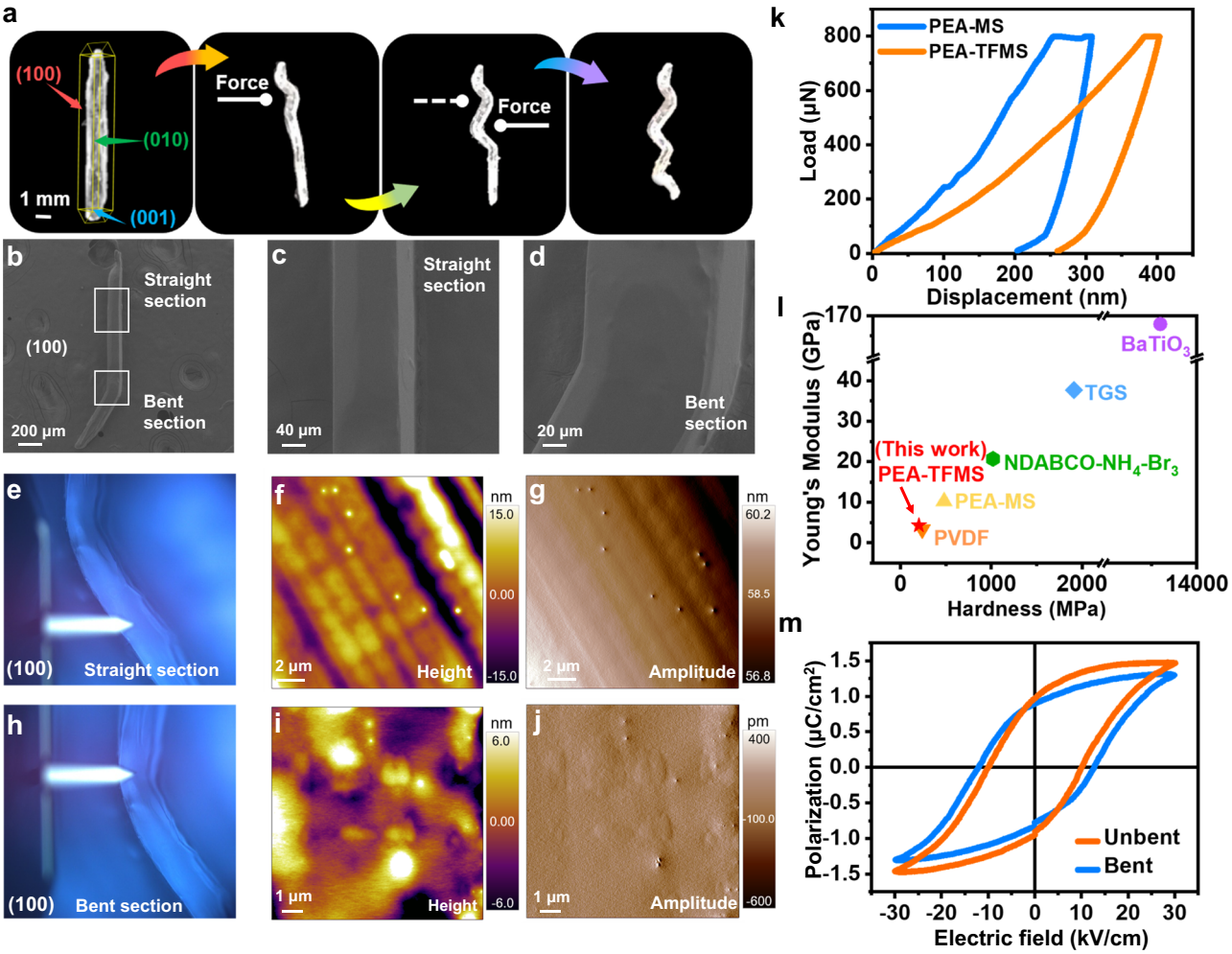

Fig. 5 | Mechanical properties and morphology of PEA-TFMS. a Pictures of progressive bending of PEA-TFMS caused by external forces. **b** Morphology and surface texture of PEA-TFMS crystal's side surface (100) visualized by SEM. SEM: scanning electron microscope. **c**, **d** Morphology and surface texture of PEA-TFMS crystal's side surface (100) on straight section (**b**) and bent section (**c**), respectively. **e** AFM measurement on the straight section of PEA-TFMS crystal's side surface (100). AFM Atomic force microscope. **f**, **g** AFM images of the straight section of PEA-TFMS crystal's side surface (100). **h** AFM measurement on the bent section of PEA-TFMS crystal's side surface (100). **i**, **j** AFM images of the bent section of PEA-TFMS crystal's side surface (100). **k** Load-displacement curves of PEA-TFMS and PEA-MS. **l** Comparison of Young's modulus (*E*) and hardness (*H*) between PEA-TFMS and several well-known ferroelectrics[32,49,50,60]. TGS triglycine sulfate. **m** Comparison of *P*-*E* hysteresis loops of unbent and bent PEA-TFMS crystal.

TFMS, we fixed the crystal on the finger joint, allowing it to dynamically change shape with the movement of the joint while maintaining a secure fit (Fig. 6i–k & Supplementary Movie 1). In order to satisfy the multi-form application, the bending test of PEA-TFMS thin film was also carried out, and the results showed that PEA-TFMS thin film was still intact after 300 times of bending cycles (Supplementary Fig. 12 & Movie 2). Therefore, the PEA-TFMS crystal can be processed into different shapes and sizes, making it easier to satisfy the designing requirements of electronic devices and demonstrating greater application potential.

Such interesting mechanical adaptability of PEA-TFMS crystal closely depended on the structural stacking arrangement and molecular interactions, which can be revealed by the "anisotropic stacking or sliding plane model" that as recognized mechanism to explain plastic deformation of organic crystals[30,51–54]. Fluorination endows PEA-TFMS with wave-like 2D hydrogen bonding networks while adjacent hydrogen bonding layers are supported through weaker intermolecular interactions, forming the significant anisotropy in the strength of interactions in the orthogonal direction. Meanwhile, the weaker interactions are assembled to form low-energy slip planes perpendicular to [010] direction, which is conducive to a relative slip of ionic layers proceeding along this direction, resulting in anisotropic deformation from external stimuli. Moreover, the distance between adjacent hydrogen bond layers of PEA-TFMS is more than twice that of PEA-MS (Supplementary Fig. 13a, b). In view of this, we calculated the cell void occupancy rate of PEA-MS and PEA-TFMS. The results indicate that the cell void occupancy rate of PEA-TFMS is 36.29%, higher than that of PEA-MS (34.86%) (Supplementary Fig. 13c, d). Therefore, fluorination increases the cell void occupancy and enhances the freedom of ionic motions, both of which facilitating the plasticity of PEA-TFMS. As shown in Fig. 6l, when PEA-TFMS crystal is subjected to external mechanical stress along [010] direction, the hydrogen bonding-formed molecular layers will bend respectively, leading to interlayer sliding or dislocation and thereby realizing bent on the (010) face, and keeping shape after removing external forces. For the interior of a single molecular layer, this bending process inevitably causes a change in hydrogen bonding, accompanying a shorter distance with contracting on the inside of the bending area and a distance increase with expanding on the outside. It is undoubtedly that wave-like 2D hydrogen bonding networks provides sufficient space for ion dislocations, which prevents crystal fracture during the bending process. Such structural arrangement allows molecular layers to twist along two

https://doi.org/10.1038/s41467-025-58416-y

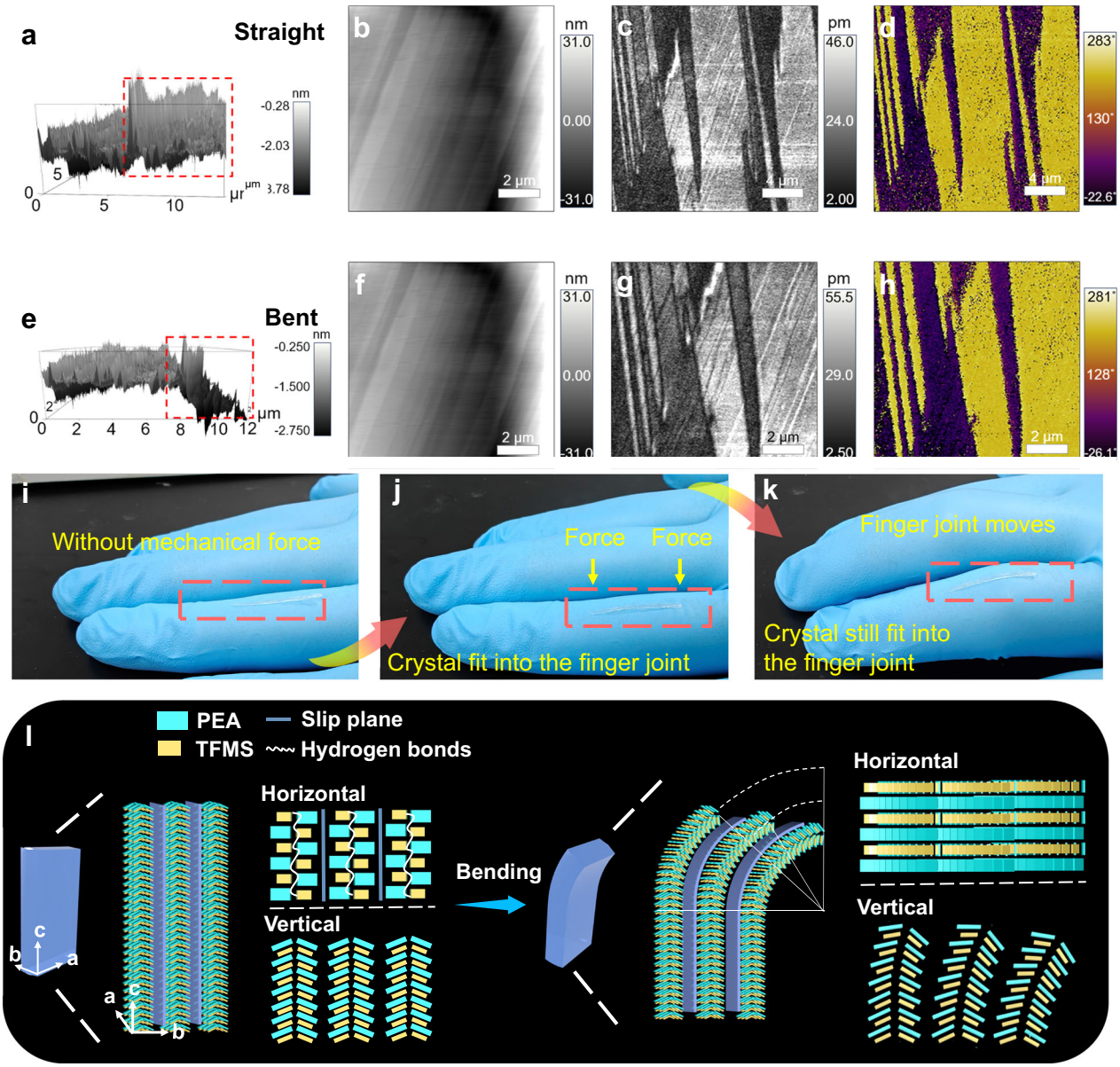

Fig. 6 | PFM images and plasticity of PEA-TFMS. a–d Morphology (**a**), height (**b**), amplitude (**c**) and phase (**d**) images of straight PEA-TFMS crystal visualized by PFM. **e–h** Morphology (**e**), height (**f**), amplitude (**g**) and phase (**h**) images of bent PEA-TFMS crystal visualized by PFM. The region in solid black boxes in (**a** and **e** represents the crystal morphology observed during PFM testing. The region in dashed red boxes indicates bending deformation occurs. **i–k** PEA-TFMS exhibit plasticity and can be fitted into the finger joint. The PEA-TFMS crystals are in the red dashed boxes. **l** Schematic diagram of the mechanism for the plastic bending process of PEA-TFMS.

different directions in (010) face, realizing helical-like deformation (Fig. 6l & Supplementary Figs. 7b and 14).

Discussion

Our study demonstrated that the fluorination implement on anionic parts realize both ferroelectricity and mechanically deformable flexibility, as a breakthrough of organic ferroelectric crystals as well as crystal engineering. Fluorination on anionic parts enables the PEA-TFMS with a wave-like 2D hydrogen bonding network to align the dipoles and reorganize anisotropy of molecular interactions, which not only induce switchable spontaneous polarization but also endow the PEA-TFMS with interesting plasticity. This successful example provides a reliable route to pursue mechanically adaptive ferroelectrics in organic crystals with plasticity, to finally reach the aim of mechanically flexible devices. It can be foreseen that organic ferroelectric crystals with various mechanical functions may be available in the near future.

Methods

Single-crystal X-ray diffraction (SXRD) determination

Single-crystal diffraction data of PEA-TFMS at LTP and HTP were collected using a Bruker D8 venture with Mo-Kα radiation (λ = 0.71073 Å) and Cu-Kα radiation (λ = 1.54184 Å), respectively. Among the other crystals, excluding PEA-MS which utilize Mo-Kα radiation, the rest employ Cu-Kα radiation. Refinement and reduction were carried out by APEX-III software. Crystallography data of the single crystals was solved and refined with the SHELXT and OLEX2 1.5 software packages, and all the non-hydrogen atoms were anisotropically manipulated.

Powder X-ray diffraction (PXRD)

Powder X-ray diffraction measurements were performed on a Rigaku D/MAX 2000 PC X-ray diffractometer at room temperature in the degree range of 5–40° at room temperature. Simulated powder patterns of samples were calculated by Mercury software package with

crystallographic information file. The PXRD patterns of PEA-MS and PEA-TFMS measured at room temperature were shown in Supplementary Fig. 15.

Thermal and second harmonic generation (SHG) measurements

The DSC measurements of PEA-TFMS powder were executed using NETZSCH-214 instrument at nitrogen atmosphere with the experimental rate being 20, 10 and 5 K/min. SHG data was collected by an unexpanded laser beam with low divergence (pulsed Nd:YAG at a wavelength of 1064 nm, 5 ns pulse duration, 1.6 MW peak power, 10 Hz repetition rate), whose instrument model is Ins 1210058, INSTEC Instruments, while the laser is Vibrant 355 II, OPOTEK.

Dielectric and *P-E* hysteresis loops measurements

The temperature-dependent permittivity was measured with a TH2828A impedance analyzer and the measurement of the *P-E* hysteresis loop was conducted on a commercial equipment Radiant Precision Premier II with operation frequency of 50 Hz. The method employed to test the ferroelectric properties is Sawyer-Tower method. The samples for dielectric and *P-E* hysteresis loops measurements are same. The crystal is precisely cut to the appropriate size (Supplementary Fig. 16), and the surfaces perpendicular to its polar axis are coated with silver conductive paste. Subsequently, the crystal is utilized to fabricate electrode for measurement following the drying of the silver conductive paste. The polarization fatigue was obtained after more than 10^7 cycles of polarization switching with Sawyer-Tower method.

Preparation of thin film

The thin film was prepared by evaporating methanol solution of PEA-TFMS. The precursor solution was prepared by dissolving 100 mg of PEA-TFMS in 2 mL of methanol. The thin films were obtained from the precursor solution (50 µL) dripped on a clean indium-tin-oxide (ITO) coated glass/polyethylene terephthalate (PET) substrate at room temperature. The diffraction data for PEA-TFMS thin film was shown in Supplementary Fig. 17.

SEM, AFM and PFM measurements

The morphology of PEA-TFMS crystal was observed by field emission scanning electron microscope (GEminiSEM 300, Zeiss) and atomic force microscope (Vero AFM, Asylum Research). The PFM measurement was carried out on a resonant-enhanced PFM (MFP3D, Asylum Research) with conductive Pt/Ir-coated silicon probes (EFM, Nanoworld), which is based on a commercial piezoresponse force microscope (Oxford instrument, Cypher ES) with high-voltage package and in-situ heating stage. PFM measurements were performed at the contact-resonance frequency of approximately 740 kHz and a 2 V a.c. drive voltage was applied to the PFM probes in PFM switching spectroscopy measurements.

Raman spectroscopy

The Raman spectroscopy measurements of straight and bent PEA-TFMS crystals were executed using Renishaw inVia Reflex instrument at room temperature in the range of 200–3800 cm^{-1}. The excitation wavelength is 633 nm (He–Ne laser).

Nanoindentation method

The nanoindentation measurements of PEA-TFMS and PEA-MS were conducted using a Bruker Hysitron TI Premier nanoindentation instrument. A standard diamond Berkovich probe with a radius of curvature of 150 nm was employed as the test probe.

Computational calculations

The DFT calculations were performed by using Vienna Ab Initio Simulation Package (VASP)[55]. The projector-augmented wave method (PAW)[56] and Perdew-Burke-Ernzerhof (PBE)[57] functional were used to describe the electron-ion and the exchange-correlation interactions respectively. Ferroelectric polarization calculation was based on the Berry phase method developed by Kingsmith and Vanderbilt[58]. The calculation was based on the crystal structures without structural relaxation. The cutoff energy of 550 eV and $3 \times 1 \times 4$ *k*-point meshed were used for all simulations. And the energy convergence criteria were set to 10^{-6} eV.

Data availability

The crystal structures generated in this study have been deposited in the Cambridge Crystallographic Data Centre with reference number of CCDC 2333578-2333583 and 2401492 [www.ccdc.cam.ac.uk/data_request/cif]. Source data is provided with this paper (reference[59]) and in the figshare database under accession code [https://doi.org/10.6084/m9.figshare.28423577]. Source data are provided with this paper.

References

1. Zhao, P. et al. High-Performance Relaxor Ferroelectric Materials for Energy Storage Applications. *Adv. Energy Mater.* **9**, 1803048 (2019).
2. Vijayakanth, T. et al. A Ferroelectric Aminophosphonium Cyanoferrate with a Large Electrostrictive Coefficient as a Piezoelectric Nanogenerator. *Angew. Chem. Int. Ed.* **62**, e202214984 (2023).
3. Noel, P. et al. Non-volatile electric control of spin-charge conversion in a $SrTiO_3$ Rashba system. *Nature* **580**, 483–486 (2020).
4. Gao, L. et al. Intrinsically elastic polymer ferroelectric by precise slight cross-linking. *Science* **381**, 540–544 (2023).
5. Scott, J. F. Applications of modern ferroelectrics. *Science* **315**, 954–959 (2007).
6. Zhang, H.-Y. et al. Biodegradable ferroelectric molecular crystal with large piezoelectric response. *Science* **383**, 1492–1498 (2024).
7. Valasek, J. Piezo-Electric and Allied Phenomena in Rochelle Salt. *Phys. Rev.* **17**, 475–481 (1921).
8. Abel, S. et al. Large Pockels effect in micro-and nanostructured barium titanate integrated on silicon. *Nat. Mater.* **18**, 42–47 (2019).
9. Li, J. L. et al. Lead zirconate titanate ceramics with aligned crystallite grains. *Science* **380**, 87–93 (2023).
10. Park, C., Lee, K., Koo, M. & Park, C. Soft Ferroelectrics Enabling High-Performance Intelligent Photo Electronics. *Adv. Mater.* **33**, 2004999 (2021).
11. Hu, Y. et al. Bond engineering of molecular ferroelectrics renders soft and high-performance piezoelectric energy harvesting materials. *Nat. Commun.* **13**, 5607 (2022).
12. Liao, W.-Q. et al. Optically Induced Ferroelectric Polarization Switching in a Molecular Ferroelectric with Reversible Photoisomerization. *Adv. Sci.* **8**, 2102614 (2021).
13. Harada, J. et al. Ferroelectric Ionic Molecular Crystals with Significant Plasticity and a Low Melting Point: High Performance in Hot-Pressed Polycrystalline Plates and Melt-Grown Crystalline Sheets. *Angew. Chem. Int. Ed.* **62**, e202215286 (2023).
14. Jiao, S. et al. Metal-free chiral molecular ferroelectric photovoltaics. *Chem. Eng. J.* **477**, 146805 (2023).
15. Hu, Y. et al. Chemically driven energetic molecular ferroelectrics. *Nat. Commun.* **12**, 5696 (2021).
16. Fu, D.-W. et al. Diisopropylammonium Bromide Is a High-Temperature Molecular Ferroelectric Crystal. *Science* **339**, 425–428 (2013).
17. Awad, W. M. et al. Mechanical properties and peculiarities of molecular crystals. *Chem. Soc. Rev.* **52**, 3098–3169 (2023).
18. Panda, M. K. et al. Spatially resolved analysis of short-range structure perturbations in a plastically bent molecular crystal. *Nat. Chem.* **7**, 65–72 (2015).
19. Lee, S. et al. Shape memory in self-adapting colloidal crystals. *Nature* **610**, 674–679 (2022).

20. Ai, Y. et al. Biodegradable Ferroelectric Molecular Plastic Crystal $HOCH_2(CF_2)_7CH_2OH$ Structurally Inspired by Polyvinylidene Fluoride. *Adv. Mater.* **36**, 2405981 (2024).
21. Wang, B. et al. Achievement of a giant piezoelectric coefficient and piezoelectric voltage coefficient through plastic molecular-based ferroelectric materials. *Matter* **5**, 1296–1304 (2022).
22. Harada, J. et al. Directionally tunable and mechanically deformable ferroelectric crystals from rotating polar globular ionic molecules. *Nat. Chem.* **8**, 946–952 (2016).
23. Ding, R. et al. Effective Piezo-Phototronic Enhancement of Flexible Photodetectors Based on 2D Hybrid Perovskite Ferroelectric Single-Crystalline Thin-Films. *Adv. Mater.* **33**, 2101263 (2021).
24. Peng, B. et al. Phase-transition induced giant negative electrocaloric effect in a lead-free relaxor ferroelectric thin film. *Energy Environ. Sci.* **12**, 1708–1717 (2019).
25. Han, S. et al. Soft Multiaxial Molecular Ferroelectric Thin Films with Self-Powered Broadband Photodetection. *J. Am. Chem. Soc.* **144**, 20315–20322 (2022).
26. Catalano, L. et al. Dual-Mode Light Transduction through a Plastically Bendable Organic Crystal as an Optical Waveguide. *Angew. Chem. Int. Ed.* **57**, 17254–17258 (2018).
27. Das, S., Saha, S., Sahu, M., Mondal, A. & Reddy, C. M. Temperature-Reliant Dynamic Properties and Elasto-Plastic to Plastic Crystal (Rotator) Phase Transition in a Metal Oxyacid Salt. *Angew. Chem. Int. Ed.* **61**, e202115359 (2022).
28. Das, S., Mondal, A. & Reddy, C. M. Harnessing molecular rotations in plastic crystals: a holistic view for crystal engineering of adaptive soft materials. *Chem. Soc. Rev.* **49**, 8871–9250 (2020).
29. Wei, C. et al. Flexible molecular crystals for optoelectronic applications. *Chem. Soc. Rev.* **53**, 3687–3713 (2024).
30. Krishna, G. R., Devarapalli, R., Lal, G. & Reddy, C. M. Mechanically Flexible Organic Crystals Achieved by Introducing Weak Interactions in Structure: Supramolecular Shape Synthons. *J. Am. Chem. Soc.* **138**, 13561–13567 (2016).
31. Saha, S. & Desiraju, G. R. Crystal Engineering of Hand-Twisted Helical Crystals. *J. Am. Chem. Soc.* **139**, 1975–1983 (2017).
32. Matthias, B. T., Miller, C. E. & Remeika, J. P. Ferroelectricity of Glycine Sulfate. *Phys. Rev.* **104**, 849–850 (1956).
33. Qiu, H. et al. Fluorination Strategy Towards Symmetry Breaking of Boron-centered Tetrahedron for Poly-fluorinated Optical Crystals. *Angew. Chem. Int. Ed.* **63**, e202316194 (2024).
34. Mykhailiuk, P. K. Fluorinated Pyrazoles: From Synthesis to Applications. *Chem. Rev.* **121**, 1670–1715 (2021).
35. Zhang, C. et al. Biological Utility of Fluorinated Compounds: from Materials Design to Molecular Imaging, Therapeutics and Environmental Remediation. *Chem. Rev.* **122**, 167–208 (2022).
36. Gao, B. et al. Bifluoride-catalysed sulfur(VI) fluoride exchange reaction for the synthesis of polysulfates and polysulfonates. *Nat. Chem.* **9**, 1083–1088 (2017).
37. Reichenbacher, K., Suss, H. I. & Hulliger, J. Fluorine in crystal engineering-"the little atom that could". *Chem. Soc. Rev.* **34**, 22–30 (2005).
38. Ai, Y., Lv, H.-P., Wang, Z.-X., Liao, W.-Q. & Xiong, R.-G. H/F substitution for advanced molecular ferroelectrics. *Trends Chem.* **3**, 1088–1099 (2021).
39. Zhang, Z.-X. et al. Organic-Inorganic Hybrid Ferroelectric and Antiferroelectric with Afterglow Emission. *Angew. Chem. Int. Ed.* **63**, e202319650 (2024).
40. Deng, W.-F. et al. Inversion of Molecular Chirality Associated with Ferroelectric Switching in a High-Temperature Two-Dimensional Perovskite Ferroelectric. *J. Am. Chem. Soc.* **145**, 5545–5552 (2023).
41. Xu, H. et al. A Metal-Free Molecular Antiferroelectric Material Showing High Phase Transition Temperatures and Large Electrocaloric Effects. *J. Am. Chem. Soc.* **143**, 14379–14385 (2021).
42. Tang, Y. Y. et al. Organic Ferroelectric Vortex-Antivortex Domain Structure. *J. Am. Chem. Soc.* **142**, 21932–21937 (2020).
43. Akutagawa, T. et al. Ferroelectricity and polarity control in solid-state flip-flop supramolecular rotators. *Nat. Mater.* **8**, 342–347 (2009).
44. Gao, J. X., Zhang, W. Y., Wu, Z. G., Zheng, Y. X. & Fu, D. W. Enantiomorphic Perovskite Ferroelectrics with Circularly Polarized Luminescence. *J. Am. Chem. Soc.* **142**, 4756–4761 (2020).
45. Hayashi, S., Yamamoto, S.-y, Takeuchi, D., Ie, Y. & Takagi, K. Creating Elastic Organic Crystals of π-Conjugated Molecules with Bending Mechanofluorochromism and Flexible Optical Waveguide. *Angew. Chem. Int. Ed.* **57**, 17002–17008 (2018).
46. Ghosh, S. & Reddy, C. M. Elastic and Bendable Caffeine Cocrystals: Implications for the Design of Flexible Organic Materials. *Angew. Chem. Int. Ed.* **51**, 10319–10323 (2012).
47. Oliver, W. C. & Pharr, G. M. An improved technique for determining hardness and elastic modulus using load and displacement sensing indentation experiments. *J. Mater. Res.* **7**, 1564–1583 (1992).
48. Karothu, D. P. et al. Global Analysis of the Mechanical Properties of Organic Crystals. *Angew. Chem. Int. Ed.* **61**, e202113988 (2022).
49. Ryu, S. S., Kim, H. T., Kim, H. J. & Kim, S. Characterization of mechanical properties of $BaTiO_3$ ceramic with different types of sintering aid by nanoindentation. *J. Ceram. Soc. Jpn.* **117**, 811–814 (2009).
50. Zhang, Z. X. et al. The First Chiro-Inositol Organosilicon Ferroelectric Crystal. *Angew. Chem. Int. Ed.* **61**, e202210809 (2022).
51. Wang, Z. et al. Mechanoresponsive Flexible Crystals. *JACS Au* **4**, 279–300 (2024).
52. Reddy C. M. et al. Structural basis for bending of organic crystals. *Chem. Commun*. 3945–3947 https://doi.org/10.1039/b505103g (2005).
53. Reddy, C. M., Kirchner, M. T., Gundakaram, R. C., Padmanabhan, K. A. & Desiraju, G. R. Isostructurality, polymorphism and mechanical properties of some hexahalogenated benzenes: the nature of halogen...halogen interactions. *Chem.-Eur. J.* **12**, 2222–2234 (2006).
54. Reddy, C. M., Krishna, G. R. & Ghosh, S. Mechanical properties of molecular crystals-applications to crystal engineering. *Cryst. Eng. Comm.* **12**, 2296–2314 (2010).
55. Kresse, G. & Furthmüller, J. Efficiency of ab-initio total energy calculations for metals and semiconductors using a plane-wave basis set. *Comput. Mater. Sci.* **6**, 15–50 (1996).
56. Blochl, P. E. Projector augmented-wave method. *Phys. Rev. B* **50**, 17953–17979 (1994).
57. Perdew, J. P., Ernzerhof, M. & Burke, K. Rationale for mixing exact exchange with density functional approximations. *J. Chem. Phys.* **105**, 9982–9985 (1996).
58. King-Smith, R. D. & Vanderbilt, D. Theory of polarization of crystalline solids. *Phys. Rev. B* **47**, 1651–1654 (1993).
59. Huang, P.-Z. et al. Related Properties of a Ferroelectric Data sets. https://doi.org/10.6084/m9.figshare.28423577 (2025).
60. Zhang, H. et al. Large Piezoelectric Response in a Metal-Free Three-Dimensional Perovskite Ferroelectric. *J. Am. Chem. Soc.* **145**, 4892–4899 (2023).

Acknowledgements

This work was supported by the National Natural Science Foundation of China (grant 22375182 (Y.Z.), 22371258 (D.-W.F.), 22405243 (Z.-X.Z.) and 21991141 (D.-W.F.)), the Natural Science Foundation of Zhejiang Province (LZ24B010001 (Y.Z.) and (LQN25B010003 (Z.-X.Z.)) and the Science and Technology Plan Project of Jinhua (2024-1-060)(Z.-X.Z.).

Author contributions

Z.-X.Z., Y.Z. and D.-W.F. conceived the project. Y.Z. and D.-W.F. designed the experiments. Z.-Q.L. proposed the theoretical mechanisms. P.-Z.H.,

Z.-Q.L. and Z.-X.Z. prepared the samples and performed the dielectric, DSC, single crystal structure measurements and analysis. Y.Z., Z.-Q.L., and L.-K.Y. performed *P-E* loops measurements and analysis. H.-F.N. performed the DFT calculations. H.-F.N., Z.-Q.L. and L.-K.Y. performed PFM measurements. C.-F.W. and D.-W.F. contributed to PFM analysis. B. Z. performed SHG measurements. J.-Q.L., G.T. and Q.-Q.J. contributed to data analysis and illustrations. Z.-X.Z., P.-Z.H. and Z.-Q.L. wrote the manuscript, with inputs from all other authors.

Competing interests
The authors declare no competing interests.

Additional information
Supplementary information The online version contains supplementary material available at https://doi.org/10.1038/s41467-025-58416-y.

Correspondence and requests for materials should be addressed to Zhi-Xu Zhang, Yi Zhang or Da-Wei Fu.

Peer review information *Nature Communications* thanks the anonymous reviewers for their contribution to the peer review of this work. A peer review file is available.